International Astronautical Congress, Milan, Italy, 14-18 October 2024.

IAC-24-D2-6-9-x87783

Robust Fault Detection and Isolation algorithms for TVC systems: An experimental test

Stefano Farì[a]*, **David Seelbinder**[a], **Stephan Theil**[a], **Pedro Simplicio**[b]

[a] *German Aerospace Center (DLR), Department of Navigation and Control Systems, Institute of Space Systems, Robert-Hooke-Str. 7, 28359 Bremen, Germany.*
E-mail: stefano.fari@dlr.de, david.seelbinder@dlr.de, stephan.theil@dlr.de

[a] *Aurora Technology for the European Space Agency (ESA), Keplerlaan 1, 2201 AZ Noordwijk, The Netherlands*
E-mail: pedro.simplicio@ext.esa.int

* Corresponding author

Abstract

This paper addresses the development and hardware testing of Fault Detection and Isolation (FDI) algorithms for Thrust Vector Control (TVC) systems driven by Electro-Mechanical Actuators (EMAs). Reusable rockets can primarily benefit from such algorithms because assessing any TVC degradation during a mission is essential to timely trigger recovery actions. Furthermore, monitoring TVC sensor can also evidence the presence of degradation across multiple flights. We propose a suitable FDI architecture and test it on a dedicated Hardware-In-the-Loop (HIL). The goal is to ensure that nominal and faulty conditions can be correctly discerned. This study employs a model-based FDI approach that relies on a nullspace computation, which already achieved a high TRL and a relevant track of record. The algorithms are synthesized to be robust against disturbance, like friction and vehicle-induced loads. To this purpose, a detailed modeling of the system, as well as fault detectability and isolability analyses are provided.

Nomenclature

β	TVC deflection angle (rad)
η	EMA efficiency (-)
θ	EMA motor angular position (rad)
b_e	Nozzle damping coefficient (N.m.s/rad)
b_m	Electrical motor viscous coefficient (N.m.s/rad)
J_m, J_e	Motor and nozzle moment of inertia (kg.m^2)
k_e	Electrical motor back-EMF constant (rad/s/V)
K_p, K_i	Electrical motor current PI controller gains (-)
k_s	TVC structural stiffness coefficient (N/m)
k_t	Electrical motor torque constant (N.m/A)
L_a	TVC lever arm (m)
L_g	EMA transmission ratio (m/rad)
L_m	Electrical motor inductance (Henry)
R_m	Electrical motor resistance (Ohm)
y_a	EMA stroke displacement (m)
f, r	Fault and residual signals
$G(s)$	Generic plant dynamics (transfer function matrix)
$Q(s)$	Generic residual generator (transfer function matrix)
S	Generic fault signature matrix

1. Introduction

Space transportation is undergoing a significant transformation, with substantial efforts being invested worldwide in the development of reusable launch vehicles. Reusable rockets are currently golden assets for the few private or governmental entities withholding the know-how to operate them [1]. This reusable rocket 'technological divide' is gradually being bridged by private and public initiatives, where efforts are focused on demonstrating the functionality and reliability of initial products or prototypes. However, these efforts may not necessarily and immediately involve the development of effective strategies to determine the health status of the vehicle. For example, in a scenario where a rocket booster has been successfully launched and landed several times, we may ask: How reliable is it for another launch?

To begin answering this question, monitoring sensors

Acknowledgements: The authors are deeply thankful to Massimo Casasco, Alvaro Martinez Barrio and Irene Huertas Garcia (*European Space Agency (ESA), Keplerlaan 1, 2201 AZ Noordwijk, The Netherlands*) for their invaluable support in using and adapting the testing facilities at ESA-ESTEC.

and actuators is an important first step. The new information collected in-flight can be used to trigger fault mitigation schemes or for post-flight degradation analyses. One of the most crucial vehicle component is the Thrust Vector Control (TVC) system, which changes an engine's thrust pointing direction by diverting the hot fluids exit point. As such, the engine must have a movable part (often including a nozzle) mounted on a gimbal, driven by two translational actuators, either electro-hydraulic or fully electric. Following the need for electrification to reduce mass, cost and complexity (especially helpful in the case of a cluster of engines), we consider here only Electro-Mechanical Actuators (EMAs). Examples of EMA-based TVC systems can be found in Avio's VEGA-C rocket [2] or the new engine cluster configuration of SpaceX's Starship [3].

In this paper we focus on a methodology for online fault detection and isolation (FDI). The actuator-level TVC control system requires several measurements normally obtained via LVDT stroke displacement sensors, electric motor angular position sensors, and current sensors, to meet operational and performance requirements. Expanding upon [4], we firstly discuss the detection of additive faults affecting the measurements involved the actuator closed-loop control system. To this goal, a model-based FDI architecture based on the nullspace approach is employed. Model-based methods usually compare measurements against model predictions and generate residual signals to highlight the presence of faults. They have already found application in several sectors, like the aircraft industry [5,6], but they are new for TVC systems. Therefore, this research showcases its adaptability and potential. Furthermore the nonlinear dynamics of the EMAs, mainly due to the electric motor, the mechanical transmission, as well as the vehicle-induced loads, pose significant challenges [7].

The second part of this work focuses on the dedicated Hardware-In-the-Loop (HIL) setup used to test the FDI algorithms. All the employed hardware components are detailed. By using different TVC deflection reference profiles, the FDI filters ability to maintain a low residual magnitude in fault-free conditions and otherwise show the presence of faults when sensor readings are altered via software are tested. Additionally, we test the effective decoupling of vehicle loads and external disturbance. This finally underscores the robustness of the proposed FDI solution for reusable launch vehicle TVC systems.

In Section 2 we start with a thorough system description and the overarching problem formulation. Section 3 describes the overall FDI system architecture and Section 4 details the synthesis models. Section 5 explains the procedure for the FDI system synthesis. Section 6 describes the testbench employed for the experimental tests and presents the results. Section 7 concludes the paper.

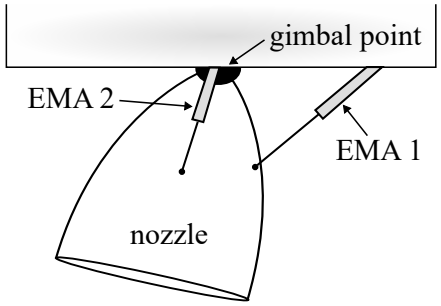

Fig. 1: Simplified view of the classically-employed thrust vectoring configuration.

2. TVC system description

The TVC actuation system must be able to tilt the engine's nozzle for a correct thrust pointing as commanded by the GNC (Guidance, Navigation and Control) algorithms. The engine's movable part (hereafter simply referred to as 'nozzle') is mounted on a gimbal system and maneuvered by EMAs acting on two perpendicular planes (Fig. 1). For a zero nozzle deflection angle on both planes, the EMAs are configured at a specific mid-way stroke to be able to extend or retract however needed. The gimbal point can be a spherical or universal joint; depending on this choice, the EMA-nozzle and EMA-vehicle skirt anchorage points must provide sufficient rotational degrees of freedom to the assembly also in conditions where both actuator strokes differ from the neutral position. The anchorage points to the engine frame and the nozzle are selected such that the closed kinematic chain has a lever arm that complies with the actuator load limits, as well as the required speed and maximum displacement operational domains. The inertia of the engine moving parts and the action-reaction forces from/to the vehicle, going under the name of Tail-Wag-Dog (TWD) and Dog-Wag-Tail (DWT) effects, are normally substantial and constitute non-negligible loads on the actuators.

An EMA-based TVC system generally includes the following hardware:

1. the engine nozzle, with its structural supports, anchorage points and mechanical joints;
2. a power source;
3. the embedded actuator control computer (ACC), in charge of controlling the EMA stroke position, thus the final nozzle deflection angle;
4. two EMAs (perpendicular to each other) to physically move the nozzle.

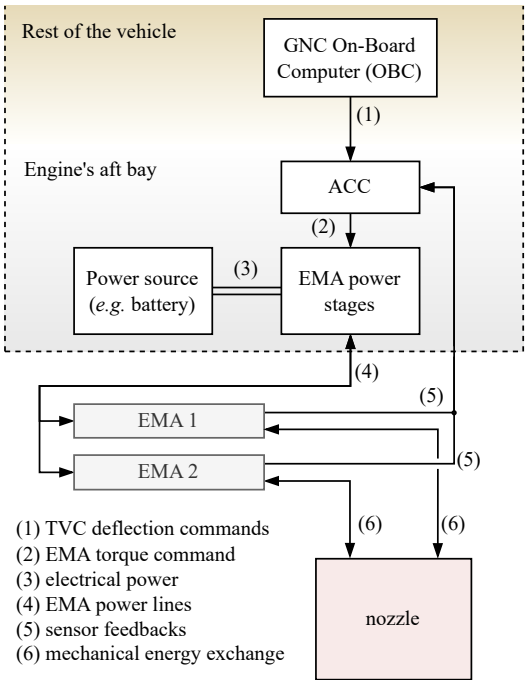

Fig. 2: High-level overall TVC architecture.

At the same time, an EMA is made by different subsystems to produce the required energy transformations and convert the electrical power into mechanical force. The three main parts are: (i) the power drive electronics (PDE), which manages the power flow between the electrical supply and actuation system; (ii) the electric motor (EM) to obtain a rotational motion from the provided electrical power; (iii) a mechanical power transmission (MPT) stage to convert the motor rotational motion into a translational motion; (iv) a set of sensors to retrieve the right quantities for the functioning of the actuator closed-loop control system.

Note that there exist many different EMA configuration options; for example, there may be a gearbox with appropriate transfer ratios to suitable modify the motor speed/torque domain. Hereafter, a direct-drive linear EMA is considered (thus no gearing elements), because of the higher geometrical integration potential, reduced friction and backlash effects, and better efficiency, stiffness and reliability. This solution has been adopted, for example, by the VEGA launch vehicle [2].

Fig. 2 depicts the high-level overall TVC architecture. The GNC on-board computer generates the commanded nozzle deflections; these commands are received by the ACC and suitably converted into a torque command based on the information received by the EMA sensors. The torque demand is managed by the EMA power stages that extract the correct amount of electrical power from the vehicle power source; it then modulates a suitable current for the electrical motors to reach the demanded performance. Lastly, the EMAs exchange mechanical energy with the nozzle, whose dynamics are influenced by its own inertial load and the external disturbance.

Measurements	Symbol
Motor current	i
EMA motor rotor position	θ
EMA stroke displacement	y_a
Force sensor	unused here
Nozzle deflection angle	β

Table 1: Measurements needed by the TVC control system.

Since there are multiple components acting in synergy within a TVC system, the problem must be properly defined. To be able to understand the FDI choices in Section 3, we need to firstly introduce the TVC control system architecture.

2.1 Control system

A schematic of a TVC control system, normally exploiting the measurements resumed in Table 1, is given in Fig. 3. The position and velocity control logic reside within the ACC. They are made of two loops in a cascade scheme: the innermost controls the EM angular velocity, whereas the outer loop controls the actuator stroke displacement, hence indirectly the nozzle angle. The EM angular velocity is usually obtained by differentiating a motor angular resolver measuring the motor rotational position. The stroke position control exploits the same motor position quantity (eventually converted into a stroke displacement), or by directly measuring the latter with a linear sensor. This scheme can be augmented to dampen-out the resonance peaks of the structure. It is possible to use a load cell at the EMA anchorage points to measure the force between EMA and nozzle. By taking a force measurement and applying a notch filter, the overall closed-loop overshoots can be reduced, like demonstrated in [9]. Another way to augment the control system is by using a direct measurement of the nozzle angular deflection[1], as explained in [8]. Despite a real sensor, to the best of the authors' knowledge, is not available into any in-use rocket, it offers many advantages for the closed loop system, which can be exploited also for FDI purposes. Since the testbench described in Section 6.1

[1]The sensing technology is currently under investigation [8].

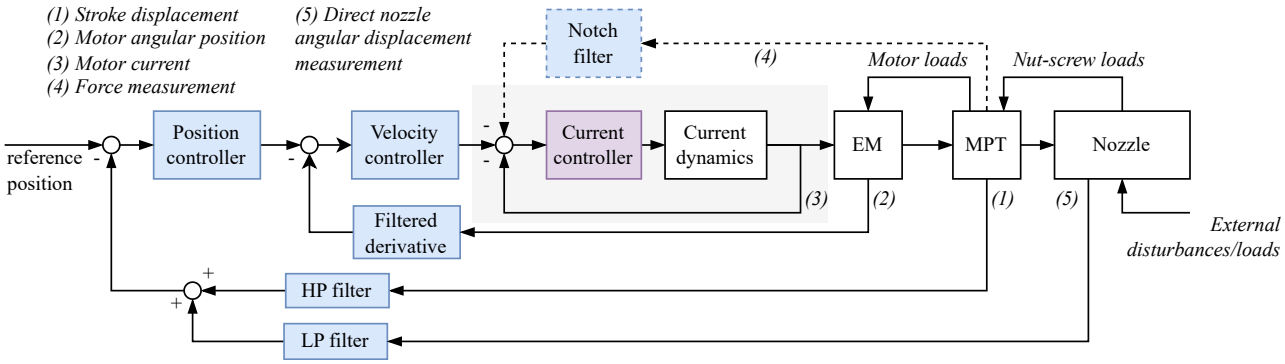

Fig. 3: Typical overall TVC control scheme (adapted from [8]).

does not have a force sensor, it will not be further included in the FDI discussion. On the contrary, a nozzle angle sensor is available.

The motor current control, instead, is normally included in the EMA power stages, so the current sensor(s) are directly embedded therein.

Since there are multiple control loop involved, the reliability of the sensors providing the necessary measurements is critical. For instance, detecting faults affecting the direct nozzle deflection measurement may lead to the elimination of the overshoot attenuation layer. On the other hand, a fault affecting the stroke displacement measurement, may lead to either a compensation of the estimated fault in the closed loop, or the discarding of the sensor itself and the feedback of the motor angular position measurement instead. The opposite applies if the faulty sensor is the one determining the motor angular speed. Anyhow, the same reasoning can be replicated if the sensor configuration differs in other setups.

3. Overview of the FDI architecture

In this Section, we discuss the architecture of the FDI system. As explained, the current control loop lives within the power stage internal hardware electronics, as well as the current sensor. It makes sense, therefore, to divide the FDI into monitoring power stage (PS) faults and mechanical assembly (MA) sensor faults which fed back into the ACC. Model-based FDI algorithms normally compare the available measurements with their expectations after a synthesis procedure based on a reference model. This is highlighted in the architecture diagram shown in Fig. 4.

3.1 FDI for power stage faults

The current control is achieved by means of a current sensor within each actuator power stage unit. In DC motors, a single current sensor usually suffices due to the straightforward nature of the current flow. However, permanent magnet synchronous motors (PMSMs) require three current sensors—one for each phase—to accurately capture the electrical activity across all phases.

To implement a complete FDI system, one must also interrogate on how to determine whether the entire unit has failed or if anomalies are affecting only the sensor(s)[2]. In fact, while and entirely faulty unit may be considered as unrecoverable, faults affecting the sensors may be mitigated by switching to sensorless control techniques, trading, in exchange, lower performance [10]. In this case, to distinguish whether a fault is affecting the unit itself or a sensor (detection and isolation of two faults), one needs an amount of sensors that is greater or equal than the number of faults, as explained in Section 5. In high-performance systems like those found in aerospace applications, hardware redundancy is typically already incorporated into the design. This means it is safe to assume the presence of redundant sensors.

The detection and isolation algorithm receives the current demand as determined by the ACC, and the two (or more) motor current measurements. The algorithm is built to provide detection and isolation on all sensors but one, that is considered as a "source of truth", and also determines if there are additive faults at whole power unit level.

Remark 1. It is anyway possible to determine faults affecting the "truthful" sensor: in fact, if the residual of all

[2]Unit failures may involve the switching components, such as IGBTs or MOSFETs, that can be experiencing overcurrent, overvoltage, and thermal stress. Thermal management failures are particularly significant, especially in reusable rockets as it is likely that there is no convection cooling because of the absence of atmospheric air. This means that if the thermal design is inefficient or if components overheat, it could lead to system failures. The proximity of these systems to the engine(s) may further exacerbate the thermal stress.

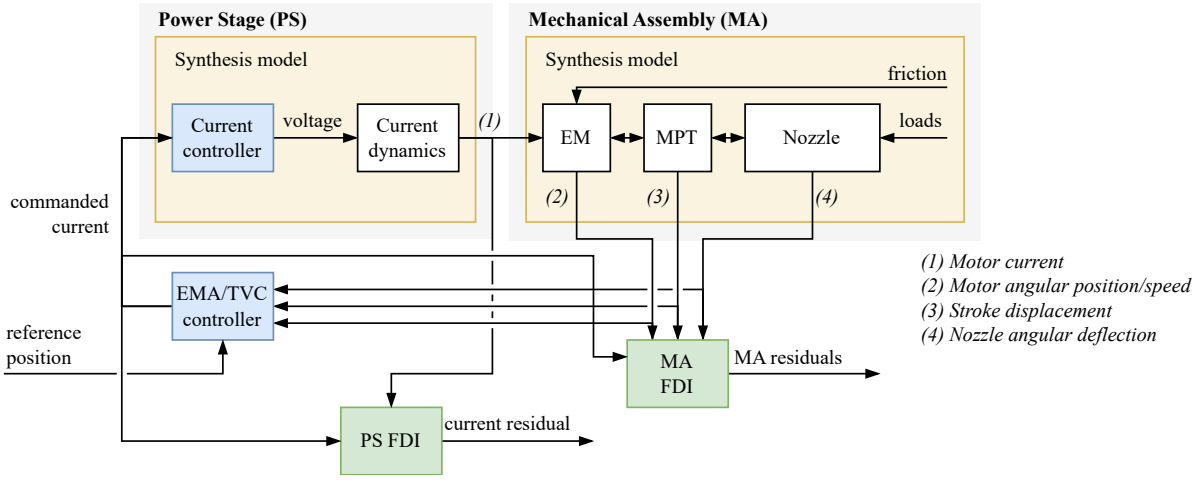

Fig. 4: Overall FDI architecture.

other monitored quantities are exceeding the set threshold, this indicates that it is the faulty one, or that other faults (accounted for) have occurred.

Note that normally the synthesis models are open-loop. In this setup a closed-loop synthesis model is considered because it aligns with the hardware capabilities of the test-bench (see Section 6.1.1).

3.2 FDI for faults at mechanical assembly level

The FDI system at mechanical assembly level is designed to involve the sensors participating in the EMA control system. The algorithms in this case receive the available mechanical measurements and the control demand, here being the current setpoint as coming from the ACC. It is possible, in fact, to neglect the current dynamics since they are at a much higher frequency than the 'mechanical' closed loop. The generated residuals are designed to show faults affecting the EMA stroke displacement, motor angular speed and nozzle deflection angle measurements.

4. TVC system modeling with faults

In this Section, we describe the synthesis models for the power stage and the mechanical assembly FDI systems.

For DC motors[3], the current dynamics is usually approximated linearly as

$$\dot{i}(t) = \frac{1}{L_m}\left[v(t) - R_m i(t) - k_e\dot{\theta}(t)\right], \tag{1}$$

[3] A similar state space also applies for PMSM; the difference resides mainly in a coordinate transformation to be done beforehand bringing the three-phase system into a fictitious DC machine.

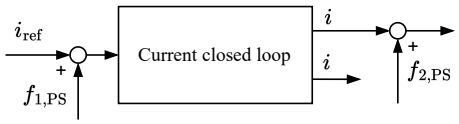

Fig. 5: The synthesis model $G_{\text{PS}}(s)$.

where i is the motor current, v the motor voltage and the term $k_e\dot{\theta}$ is the back electromotive force. By neglecting the latter and knowing that the controller is proportional-integral, we can obtain the the closed loop current transfer function:

$$\frac{i(s)}{i_{\text{ref}}(s)} = \frac{K_p s + K_i}{L_m s^2 + (R_m + K_p)s + K_i}. \tag{2}$$

By returning to the state space representation, and by adding the redundant current measurement and the fault inputs ($f_{1,\text{PS}}$,$f_{2,\text{PS}}$), we obtain:

$$\begin{aligned}
\dot{x}_{1,\text{PS}}(t) &= L_m^{-1}\left[(-K_p + R_m)x_{1,\text{PS}}(t) + K_i x_{2,\text{PS}}(t) + \ldots\right.\\
&\quad \left. + K_p\left(i_{\text{ref}}(t) + f_{1,\text{PS}}(t)\right)\right],\\
\dot{x}_{2,\text{PS}}(t) &= -x_{1,\text{PS}}(t) + \left(i_{\text{ref}}(t) + f_{1,\text{PS}}(t)\right),\\
y_{1,\text{PS}}(t) &= x_1(t) + f_{2,\text{PS}}(t),\\
y_{2,\text{PS}}(t) &= x_1(t).
\end{aligned} \tag{3}$$

States and outputs are with the symbols $x_{-,\text{PS}}$ and $y_{-,\text{PS}}$, respectively. In the Laplace domain, these dynamics are referred to as the transfer function matrix $G_{\text{PS}}(s)$, schematically represented in Fig. 5.

For the mechanical assembly FDI, we consider the two thrust vectoring planes as decoupled. The model has to

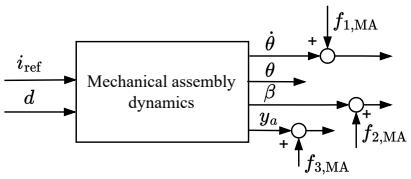

Fig. 6: The synthesis model $G_{\text{MA}}(s)$.

capture the EM, the MPT and the load part. The EM and MPT dynamics can be influenced by several nonlinear phenomena, like backlash, a preload force, friction, cogging torque or magnetic hysteresis, which are difficult to represent with linear expressions. However, it is important to capture at least the viscous motor friction, the inertial contributions of both motor and engine, and an efficiency factor [7]. If we define the state vector as $[x_{1,\text{MA}}, ..., x_{4,\text{MA}}]^T = [\dot{\theta}, \theta, \dot{\beta}, \beta]^T$, we can write the dynamics as:

$$
\begin{aligned}
\dot{x}_{1,\text{MA}}(t) &= J_a^{-1}\left[(-b_a - d_s L_g^2 \eta^{-1}) x_{1,\text{MA}}(t) + ... \right. \\
&\quad -k_s L_g^2 \eta^{-1} x_{2,\text{MA}}(t) + L_g d_s L_a \eta^{-1} x_{3,\text{MA}}(t) + ... \\
&\quad \left. + L_g k_s L_a \eta^{-1} x_{4,\text{MA}}(t) + k_t i_{\text{ref}}(t) + d(t)\right] \\
\dot{x}_{2,\text{MA}}(t) &= x_{1,\text{MA}}(t) \\
\dot{x}_{3,\text{MA}}(t) &= J_e^{-1}\left[d_s L_a L_g x_{1,\text{MA}}(t) + k_s L_a L_g x_{2,\text{MA}}(t) + ... \right. \\
&\quad \left. -(b_e + L_a^2 d_s) x_{3,\text{MA}}(t) - (k_e + L_a^2 k_s) x_{4,\text{MA}}(t)\right] \\
\dot{x}_{4,\text{MA}}(t) &= x_{3,\text{MA}}(t) \\
y_{1,\text{MA}}(t) &= x_{1,\text{MA}}(t) + f_{1,\text{MA}}(t) \\
y_{2,\text{MA}}(t) &= x_{2,\text{MA}}(t) \\
y_{3,\text{MA}}(t) &= x_{4,\text{MA}}(t) + f_{2,\text{MA}}(t) \\
y_{4,\text{MA}}(t) &= L_g x_{2,\text{MA}}(t) + f_{3,\text{MA}}(t)
\end{aligned}
\tag{4}
$$

The outputs are $[y_{1,\text{MA}}, ..., y_{4,\text{MA}}] = [\dot{\theta}, \theta, \beta, y_a]$. The term $-b_a x_{1,\text{MA}}$ is the viscous friction, k_s and d_s are stiffness and damping coefficients to link the nozzle to the EMA and correctly propagate the impressed force, b_e is a dissipative term acting on the nozzle rotation. The disturbance input d includes mainly the unmodeled friction and the vehicle-induced loads, while the sensor faults are $f_{1,\text{MA}}$, $f_{2,\text{MA}}$ and $f_{3,\text{MA}}$. Eq. (4) is named $G_{\text{MA}}(s)$ in the Laplace domain and shown in Fig. 6.

5. FDI synthesis for TVC systems

By recalling that detecting a fault detectability means 'unambiguously highlighting that a fault is present' and that fault isolability means 'knowing which fault acting on the system', we can define the synthesis objective as follows:

1. detect and isolate $f_{1,\text{PS}}$ and $f_{2,\text{PS}}$, via suitably generated residual signals;
2. detect and isolate $f_{1,\text{MA}}$, $f_{2,\text{MA}}$ and $f_{3,\text{MA}}$, via suitably generated residual signals.

5.1 Detectability, isolability and filter synthesis procedure

The synthesis is performed in continuous time and is based on the theory in [11]; afterwards, the filters are discretized for the hardware implementation. We firstly need to check the detectability and isolability of the faults. What explained here applies to both the power stage and mechanical assembly FDI syntheses. The state space expressed in Eqs. (3) and (4) can be expressed in the Laplace domain form as

$$y(s) = G_u(s)u(s) + G_d(s)d(s) + G_f(s)f(s), \tag{5}$$

where the quantities y, u, d, f mean outputs, control inputs, disturbance and faults, respectively, and G_u, G_d and G_f are the related transfer function matrices. The fault detection and isolation problem requires a residual generator which can be written as

$$r(s) = Q(s)\begin{bmatrix} y(s) \\ u(s) \end{bmatrix}, \tag{6}$$

where $r(s)$ are the residual signals (in Laplace domain) and $Q(s)$ is the filter to be synthesized, which must be stable (only poles with negative real part) and proper. The fault detection problem is addressed by producing residual signals

$$r(t) = \begin{bmatrix} r_1(t) \\ r_2(t) \\ \dots \end{bmatrix} \tag{7}$$

different than zero whenever a fault occurs. When the residual vector is sensitive to all faults and shows faults within a specific frequency domain Ω, the *strong fault detectability* property is achieved. Here, the set $\Omega = \{0\}$ is considered, thus detectability of constant faults (*i.e.* biases) is desired.

On the other hand, isolability concerns the location of the fault, hence the determination of the presence of a specific fault by associating the raise (or non raise) of a specific residual signal r_j (or more residuals) with a specific fault f_j. Normally, it is desirable that multiple occurring faults can be detected at the same time without altering the isolation capability: when this happens, the property is be

called *strong fault isolation*. For strong fault isolability one can define the fault signature matrix S where each element (k-th column, i-th row) is populated as follows:

$$S_{k,i} = \begin{cases} 1 & \text{if } R^j_{f_i}(0) \neq 0 \\ 0 & \text{if } R^j_{f_i}(s) = 0 \\ -1 & \text{if } R^j_{f_i}(0) = 0 \wedge R^j_{f_i}(s) \neq 0, \end{cases} \tag{8}$$

where $R^j_{f_i}$ is the transfer function from i-th fault to j-th residual. An entry with '1' means that when a fault occurs, the steady value of the residual output is nonzero. If the residual is not zero only "temporarily" the entry is '-1'. When the residual is not affected by the fault, '0' is set. The ideal case is when S is an identity matrix.

For the synthesis of the actual filter $Q(s)$, the solution of an Exact Fault Detection and Isolation Problem (EFDIP) [11] is hereafter considered: it allows the decoupling of both disturbances and inputs, and provides filters of minimal order, a desirable property for the final implementation into the hardware and for disturbance rejection. It is composed by three steps, at the end of which the filter $Q(s)$ gets updated as $Q(s) \leftarrow Q_K(s)...Q_1(s)$ with K being the step index.

5.1.1 Nullspace synthesis

The first step is to determine a basic fault detection filter. This basic filter can be seen as a composition of three different dynamical systems, each dealing with one fault as

$$Q(s) = [Q^1(s), Q^2(s), ..., Q^{m_f}(s)]^T, \tag{9}$$

with m_f being the number of fault inputs. Each sub-filter must achieve perfect decoupling of inputs, disturbance and all the "non-related" identified from a feasible fault signature matrix S. The structure of the filter (*i.e.* which entries are populated), as well as the pole and zero locations are the main outcome of this step. The parameters of the filter depend on the plant; the employed framework basically seeks for a dynamic system $Q(s)$ annihilating the plant structure with certain input-output decoupling criteria. If the problem to solve is is badly posed, *e.g.* it has not enough measurements, it has too many disturbance input to decouple, it has too many faults to detect, or a combination of these, then there might be no solution to it (see again [11]).

5.1.2 Update for filter minimality

The second step is meant to reduce the order of $Q(s)$ by selecting a suitable transfer function matrix $Q_2(s)$ that makes $Q_2(s)Q(s)$ have the least (McMillan) degree.

5.1.3 Filter stabilization

The last step is to eventually stabilize the filter and impose the desired dynamics. Therefore, a proper and invertible $Q_3(s)$ is designed using a left coprime factorization, such that the resulting final filter $Q_3(s)Q(s)$ has the desired dynamics.

5.2 Power stage FDI synthesis

Strong and complete fault detectability and strong fault isolability properties are guaranteed for the system in Eq. (3). The achievable strong fault specifications are in fact

$$S_{\text{PS}} = \begin{bmatrix} 1 & 0 \\ 0 & 1 \\ 1 & 1 \end{bmatrix}. \tag{10}$$

Therefore, it is possible to solve the EFDI problem with a fault-to-residual signature being the identity matrix $I_{2\times 2}$.

The synthesized filter has the following simple structure:

$$Q_{\text{PS}}(s) = \begin{bmatrix} 0 & 1 & -\frac{a_1(s+a_2)}{(s+b_1)(s+b_2)} \\ 1 & -1 & 0 \end{bmatrix} \tag{11}$$

where the inputs are the two current sensors and the current setpoint, respectively, and the parameters a_1, a_2, b_1 and b_2 are positive and linked to the $G_{\text{PS}}(s)$ pole/zero structure.

Remark 2. If there was no current sensor redundancy, the transfer function matrix for detecting and isolating faults acting on the single sensor would be as the first row of Eq. (11), with the first input being the sensor, and the second input being the current setpoint signal.

5.3 Mechanical assembly FDI synthesis

When we aim for strong fault detectability and strong fault isolability, there are several critical points to be described and addressed:

1. The presence of a disturbance to be perfectly decoupled entering in the same channel as the control input creates important constraints to the final structure of the filter. The coupling of the disturbance input d with the states in Eq. (4) cannot be changed, at it represents both the effect of the vehicle-induced loads and the unmodeled friction effects acting as external torque to the motor.
2. The quantity $\dot{\theta}$ is not effectively a measurement, since it is computed within the ACC as the filtered derivative of θ, like explained in Section 2.1.

The first point cannot be circumvented: in fact, while the external loads might eventually be addressed separately

if any force sensor was available, the motor/EMA friction can still remain an issue. In the testbench described in Section 6.1, the latter is definitely not negligible and must be considered.

Point two is more difficult to address, since it implies the following:

- by looking at Eq. (4), we cannot decide to have $f_{1,\mathrm{MA}}$ as acting on $y_{2,\mathrm{MA}}$, hence θ, rather than $y_{1,\mathrm{MA}}$, namely $\dot{\theta}$, because the EFDIP would turn unsolvable: there is no way to generate a residual for θ while keeping both $f_{2,\mathrm{MA}}$ and $f_{3,\mathrm{MA}}$ decoupled. The presence of the latter faults inhibits the use of β and y_a measurements to monitor the θ measurement;
- when we stick with Eq. (4) as is, we must recognize that the faults affecting $\dot{\theta}$ are in practice those affecting θ. As such, since θ is a quantity considered as "healty" to make the EFDIP solvable, the nullspace-based solution tries anyway to use both θ and $\dot{\theta}$ measurements for detecting and isolating $f_{1,\mathrm{MA}}$. Ultimately, this means that no $\dot{\theta}$ faults can be correctly highlighted.

Remark 3. If θ and $\dot{\theta}$ were *not* originated by the same sensor, the latter discussion would not hold because the measurements would be uncorrelated.

We propose now a solution to remedy to the aforementioned issues. At first, we augment the system $G_{\mathrm{MA}}(s)$ with the characteristics of the filtered derivative action used to obtain $\dot{\theta}$. We assume that it has a structure like:

$$\frac{\dot{\tilde{\theta}}(s)}{\theta(s)} = s\left(\frac{\gamma}{s+\gamma}\right)^2. \tag{12}$$

and we embed this into $G_{\mathrm{MA}}(s)$ to get to an augmented synthesis model $\tilde{G}_{\mathrm{MA}}(s)$. The new output $\tilde{y}_{1,\mathrm{MA}}$, then, correlates with the new $\dot{\tilde{\theta}}$ and not with $\dot{\theta}$. While not being essential, in this way we can make the synthesis aware of the two poles in $-\gamma$.

We solve now the EFDI problem. The achievable strong fault specifications are:

$$S_{\mathrm{MA}} = \begin{bmatrix} 1 & 0 & 0 \\ 0 & 1 & 0 \\ 0 & 0 & 1 \\ 1 & 1 & 0 \\ 0 & 1 & 1 \\ 1 & 0 & 1 \\ 1 & 1 & 1 \end{bmatrix}. \tag{13}$$

We opt again the fault-to-residual signature $I_{3\times 3}$. The obtained filter is

$$Q_{\mathrm{MA}}(s) = \begin{bmatrix} 1 & -\frac{c_1 s}{(s+\gamma)^2} & 0 & 0 & 0 \\ 0 & \frac{-c_2(s+c_3)(s+c_4)}{s^2+d_1 s+d_2} & 1 & 0 & 0 \\ 0 & -L_g & 0 & 1 & 0 \end{bmatrix}, \tag{14}$$

where the inputs are $\dot{\tilde{\theta}}, \theta, \beta$, y_a and i_{ref} and the coefficients all positive. This structure allows the determination of faults affecting $\dot{\theta}$ by comparing its value with the 'low-passed' derivative of θ, while faults on β are obtained by subtracting to the β measurement a scaled value of θ where the oscillating dynamics of the nozzle due to k_s and d_s different than zero are accounted for. Lastly, the residual for y_a has no dynamic as it is simply expressed as $y_a - L_g\theta$, as can be inferred from the $y_{4,\mathrm{MA}}$ equation in (4). Note that the control input i_{ref} has no effect on the residuals.

At this point, we have three residuals, say $r_{1,\mathrm{MA}}$, $r_{2,\mathrm{MA}}$ and $r_{3,\mathrm{MA}}$ where:

1. $r_{1,\mathrm{MA}}$ does not show correctly $f_{1,\mathrm{MA}}$ because of what discussed at the beginning of the Section;
2. $r_{2,\mathrm{MA}}$ and $r_{3,\mathrm{MA}}$ correctly show $f_{2,\mathrm{MA}}$ and $f_{3,\mathrm{MA}}$ separately, but not if the θ measurement is faulty.

To address this issue, we can solve one more EFDI problem to be able to determine if θ is faulty. Let us write a new state space like (4), but with the output equations as:

$$\begin{aligned} y'_{1,\mathrm{MA}}(t) &= x_{1,\mathrm{MA}}(t) + f_{1,\mathrm{MA}}(t) \\ y'_{2,\mathrm{MA}}(t) &= x_{4,\mathrm{MA}}(t) + f_{2,\mathrm{MA}}(t) \\ y'_{2,\mathrm{MA}}(t) &= x_{2,\mathrm{MA}}(t) + f_{3,\mathrm{MA}}(t) \end{aligned} \tag{15}$$

The achievable strong fault specifications are:

$$S'_{\mathrm{MA}} = \begin{bmatrix} 0 & 1 & 1 \\ 1 & 1 & 1 \end{bmatrix}. \tag{16}$$

We decide solve the EFDI problem the the residual-to-fault structure dictated by the first row $[0, 1, 1]$, as in the second row all the faults would be propagated to the residual. The result is the filter $Q'_{\mathrm{MA}}(s)$ outputting the residual $r'_{1,\mathrm{MA}}$:

$$Q'_{\mathrm{MA}}(s) = \begin{bmatrix} 0 & 1 & -\frac{c'_1(s+c'_2)}{s^2+d_1 s+d_2} & 0 \end{bmatrix}, \tag{17}$$

where the inputs are $\dot{\tilde{\theta}}$, β, y_a and i_{ref}.

Now, we can achieve the initial fault detection and isolation goals by looking at specific combinations of $r'_{1,\mathrm{MA}}, r_{2,\mathrm{MA}}$ and $r_{3,\mathrm{MA}}$, resumed in Table 2. From the Table, it is clear that we can isolate only one fault at the time. This is normally referred to as *weak isolability* and

Faulty measurement	$r_{2,\mathrm{MA}}$	$r_{3,\mathrm{MA}}$	$r'_{1,\mathrm{MA}}$
Motor angle (θ)	$\neq 0$	$\neq 0$	$= 0$
Nozzle angle (β)	$\neq 0$	$= 0$	$\neq 0$
EMA stroke position (y_a)	$= 0$	$\neq 0$	$\neq 0$

Table 2: Residual outputs in presence of a faulty measurement.

can be remedied only with the addition of more sensors, or by renouncing to detect faults on some measurement. Also note that $r_{1,\mathrm{MA}}$ has been discarded: however, it is anyway necessary to solve the first EFDIP as explained before (with $f_{1,\mathrm{MA}}$, acting on $\dot{\theta}$), to force the EFDIP solution to not include both $\dot{\theta}$ and θ measurements within the expressions of $r_{2,\mathrm{MA}}$ and $r_{3,\mathrm{MA}}$.

Remark 4. It is oftentimes possible to put multiple stroke displacement sensors in parallel, without excessive compactness sacrifices. This, or the inclusion of a force sensor, can alleviate the weak isolability issue described here.

6. Experimental results

To test the FDI algorithms, an ad-hoc testbench[4] at the ESA-ESTEC facility is used and is described hereafter. Then, we show the results in fault-free and faulty scenarios.

6.1 Testbench description

The testbench is formed by a self-contained square platform hosting several components. The combustion chamber and the nozzle mocks-up, made of steel and carbon fiber with proper in-scale MCI (Mass-Centering-Inertia) properties, are placed on a spherical joint at the middle point. The nozzle is pushed/pulled by two orthogonal EMAs. At the opposite side of the actuators there are two linear potentiometers to get an absolute measurement of the nozzle displacement. The electrical motor operates in direct current and is directly connected to an incremental quadrature encoder measuring the motor angular position. The EMA assembly is also augmented by two limit switches detecting excessive nozzle angular displacements. The main parameters are resumed in Table 3.

The testbench includes the EMA power drive electronics and an overarching microcontroller described in Sections 6.1.1 and 6.1.2. In this setup, the potentiometer measurements, which would not be present on a rocket application, are assumed to be equivalent to the quantity y_a after a suitable numerical conversion. Additionally, inside the nozzle there is another microcontroller with a 9-axes IMU running an extended Kalman filter: its purpose is to have an estimation of β to be used for FDI purposes, but no control loop augmentation.

[4]The electromechanical components of the testbench were assembled under ESA Contract 4000113551 with GMVIS Skysoft S.A.

Fig. 7: The 'Fly Safe' testbench.

Remark 5. The β determination via an IMU is performed after a calibration to eliminate misalignment offsets. Although the very indirect measurement, the resulting angle does follow rather accurately the TVC deflection obtained via a geometric conversion of the EMA stroke displacement.

6.1.1 Power drive electronics

The motor power stage is provided by a Maxon® ESCON® 70/10 module able to control both the motor current and speed. The choice of this board was dictated by the necessity to access at least the demanded and actual current for the FDI purposes.

Remark 6. The motor drive implements the current control internally and does not provide a voltage reading. This means that we must operate with the whole current closed loop, thus justifying the choices made in Section 3.

The ESCON® can also run a velocity control loop, if adequately connected to the motor encoder. Deviating

Parameter	Value	Unit
Nozzle max. deflection angle	9	deg
Nozzle max. angular velocity	15	deg/s
TVC deflection static accuracy	≈0.1	deg
TVC deflection dynamic accuracy	≈0.5	deg
Combustion chamber mass	13.3	kg
Nozzle mass	1.7	kg
Engine CoM distance from gimbal	23	cm
Motor operating voltage	24	V
Motor nominal current	6	A
Motor max. current	24	A
EMA max. speed	110	mm/s
EMA-related motor max speed	500	rpm
Encoder resolution	500	ppr
Potentiometer theoretical accuracy	0.01	mm

Table 3: Testbench main parameters.

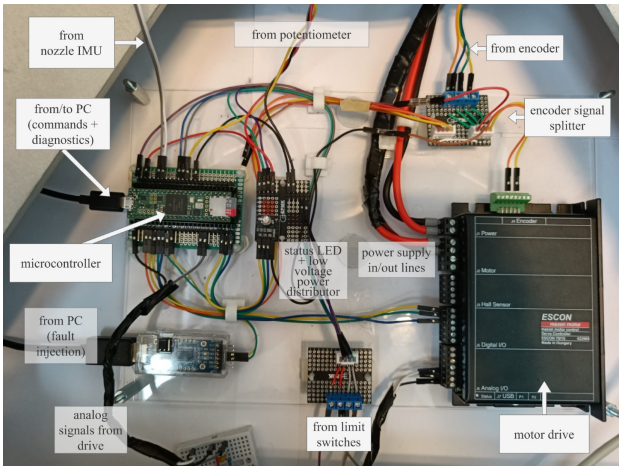

Fig. 8: The employed electronics, the power drive and auxiliary components.

from the structure in Section 2.1, but for greater simplicity, this is the adopted solution. The position control is anyhow demanded to the microcontroller.

6.1.2 TVC microcontroller

The heart of the system is the Teensy® 4.1, a compact microcontroller running a 32-bit ARM® Cortex®-M7 processor at 600 MHz. It is programmed to perform several tasks: (i) receives the TVC deflection commands from a PC via a USB serial port; (ii) receives the fault virtual signals from a PC via a hardware serial port; (iii) receives the nozzle angular displacement from an auxiliary microcontroller via a hardware serial port; (iv) receives the ESCON® current output signal as analog inputs; (v) receives the limit switches digital signals; (vi) commands the velocity setpoint to the ESCON® via PWM (Pulse-Width-Modulation) based on the internal position controller output; (vii) calibrates the platform at the beginning of an experiment; (viii) runs the FDI filters; (ix) logs all relevant data on a micro-SD card.

This microcontroller was mainly chosen for its computational power: for example, it allows log data to an SD card at a very fast rate while retaining data delayed by any factor within a big circular buffer. The chosen logging sampling time down is 500 microseconds. This is required to accurately capture the current dynamics, which are very fast (the current closed-loop critical frequency is ≈1530 rad/s.) This board is also designed to have a non-interrupted execution in most of the circumstances, *e.g.* when receiving serial commands from multiple ports. Besides that, the Teensy® can also execute several digital filters with a negligible execution footprint.

The analog input quantities, namely the currents from the ESCON® and the potentiometer voltage, are passed through a biquadratic filter with cut-off frequency of 50 Hz to reduce noise. The same filter is also applied to the derivative of the encoder ticks with cut-off frequency of 25 Hz. Together with the FDI filters, they are all scheduled to run every 1 millisecond.

Before performing any test, a system identification of the current closed loop and mechanical TVC dynamics are performed. For the first, the position and velocity loops are opened and a small current is demanded to the power stage, such that the static friction threshold is not exceeded. This avoids the generation of spurious dynamics due to the system movements. For the second, the mechanical dynamics are identified by demanding a larger current for a specific amount of time and logging the motor displacement and speed, as well as the potentiometer and IMU readings. Finally, the necessary parameters of the state spaces in Eq. (3) and Eq. (4) are obtained.

Remark 7. Ideally, one would need to perform the identification of the current dynamics without any load. With the employed testbench, this would have resulted in a complete dismantling of the mechanical transmission, which was deemed as unpractical.

Remark 8. The faults are not physically injected in the system, but simulated by altering the signals within the microcontroller, which receives the virtual faults from a PC. This means that none of the control loops would effectively react to a fault injection.

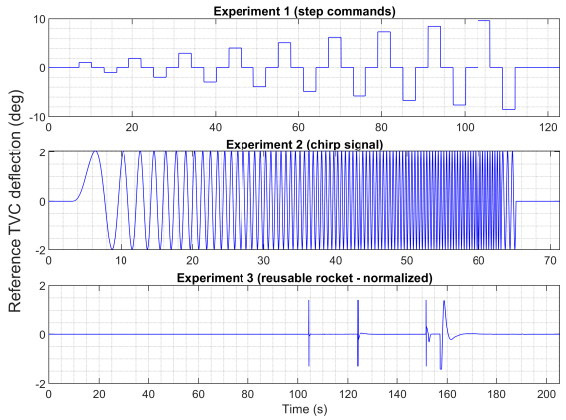

Fig. 9: Reference TVC deflection for the three experiments.

Note that in this paper we do not make assumptions on what can be a suitable threshold to compare the residual against. However, we provide an indication on how to assess if the residual is "small enough" to assess the FDI performance.

6.2 Fault-free scenarios

The following position reference profiles are considered to assess the FDI performance:

- Experiment #1: step commands with incremental amplitude;
- Experiment #2: sine sweep (up to 1.5 Hz);
- Experiment #3: profile of a real reusable rocket end-to-end mission.

The three reference TVC deflections are in Fig. 9. Note that the setpoint commands are effectively given in encoder ticks; in the Figure they have been transformed in TVC deflection angle for clarity. In this transformation, the other TVC axes (that is not moving) is considered, and therefore the conversion outputs a non-symmetrical profile. The rocket experiment is divided in three phases: ascent, boostback, aerodynamic re-entry and landing. However, only the boostback (between 100s and 130s) and landing (after 160s) demand a high TVC deflection value. The latter has been normalized to an arbitrary value due to confidentiality reasons.

All the logged experiments include load disturbances manually introduced by the operator, therefore completely unknown. The current measurement $y_{2,\mathrm{PS}}$ is generated by adding a 10% bias to $y_{1,\mathrm{PS}}$ and more noise.

Figs. 10 to 12 show the residual behavior considering Experiment #1. To understand if the residual values are acceptably small, we note that the static friction threshold for the EMA is ≈1A. This means that the fault detection sensitivity is better checked on residual values that are larger than 1A. Experiment #3 (Fig. 12) shows high peak values during certain phases of the flight. These peaks are to be smoothed by a properly tuned fault evaluation logic [11, 12].

We analyze now the residual generators $r'_{1,\mathrm{MA}}, r_{2,\mathrm{MA}}$ and $r_{3,\mathrm{MA}}$ for the mechanical assembly from Figs. 13 to 15. For all the three experiments, the residuals show a very low value. To have a magnitude for comparison, the motor maximal speed is ≈±52.35 rad/s, the TVC maximal deflection is ±0.157rad and the maximal potentiometer travel is ≈±32mm. The r_2 residual in Fig. 13 shows that a growing β amplitude corresponds to a residual increase. This is justifiable considering that no TVC axes cross-coupling compensation is included. The values recorded from the potentiometer, emulating y_a always include a systematic bias that is detected within the $r_{3,\mathrm{MA}}$ signal. This is due to the mechanical assembly tolerances and the sensitivity of the potentiometer to small variations because of the geometrical integration and the relatively high electromagnetic noise that the analog instrument and its wiring are subject to. All these factors produce also a deviation from zero of $r'_{1,\mathrm{MA}}$, as expected from Eq. (17).

6.3 Faulty scenarios

To analyze the residual behavior in presence of faults, we artificially inject bias faults. We only consider the sine excitation for conciseness reasons and for being the most frequency-rich TVC setpoint.

For the power stage FDI, we consider a bias of 3A for both $f_{1,\mathrm{PS}}$ (related with a power unit faults) and $f_{2,\mathrm{PS}}$ (related with the first current sensor faults). The second fault is injected 10 seconds after the first, to better show the isolation capability of the system. In Fig. 16 we see how the both residuals are capable of correctly highlighting the presence of faults. The first residual shows an inverted sign with respect to the fault (see Eq. (11)); this is not an issue since the residual evaluation schemes normally consider just its norm. Fig. 17 repeats the experiments by injecting a 3A offset to the second current sensor $y_{2,\mathrm{PS}}$, considered as "healthy" at the synthesis stage: in this case, both residuals raise, implicitly highlighting the presence of a fault in $y_{2,\mathrm{PS}}$.

In Figs. 18 and 19, the results for the mechanical assembly FDI system are shown. Fig. 18 shows the Experiment #2 when a bias of 2deg is injected in the β measurement at a time of 10 seconds. Successively, at 20 seconds, a 15mm fault is injected into the y_a measurement. It is

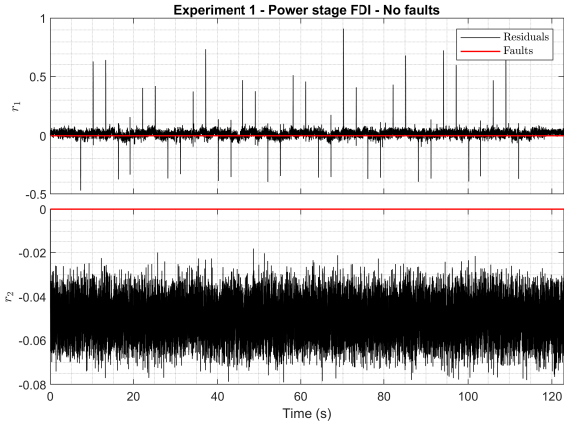

Fig. 10: Power stage residual signals (Experiment #1) in a fault-free scenario.

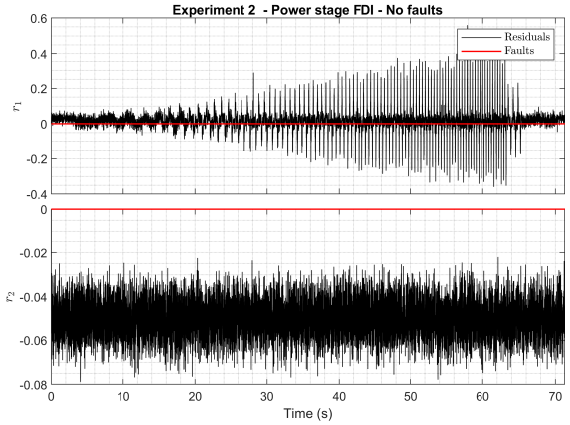

Fig. 11: Power stage residual signals (Experiment #2) in a fault-free scenario.

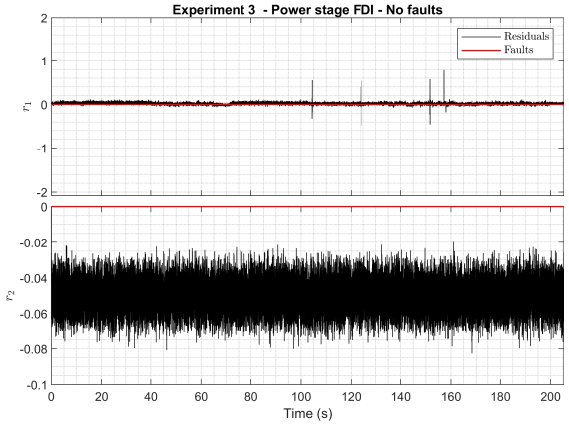

Fig. 12: Power stage residual signals (Experiment #3) in a fault-free scenario.

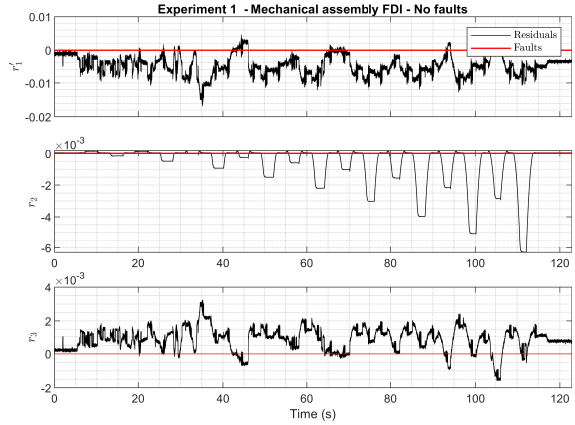

Fig. 13: Mechanical assembly residual signals (Experiment #1) in a fault-free scenario.

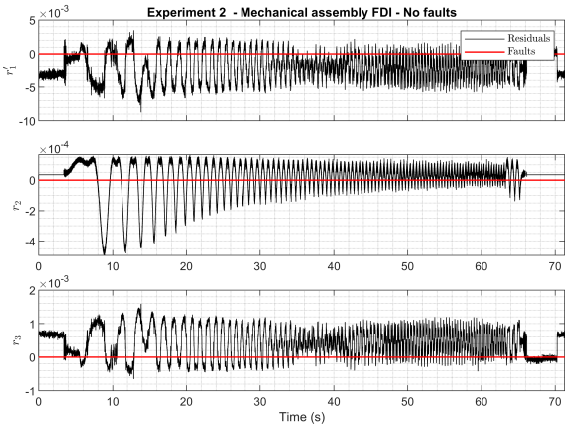

Fig. 14: Mechanical assembly residual signals (Experiment #2) in a fault-free scenario.

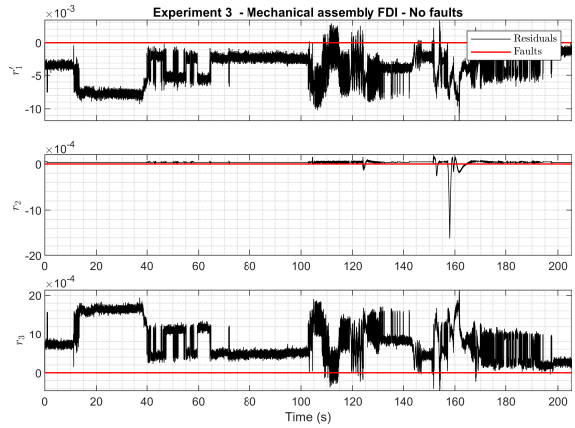

Fig. 15: Mechanical assembly residual signals (Experiment #3) in a fault-free scenario.

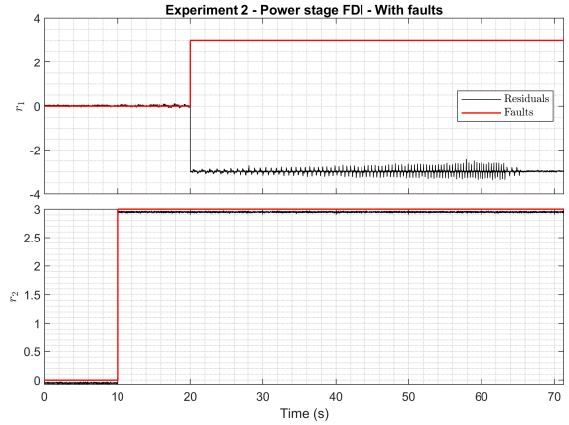

Fig. 16: Power stage residual signals (Experiment #2) in presence of bias faults affecting both the entire unit and the first current sensor.

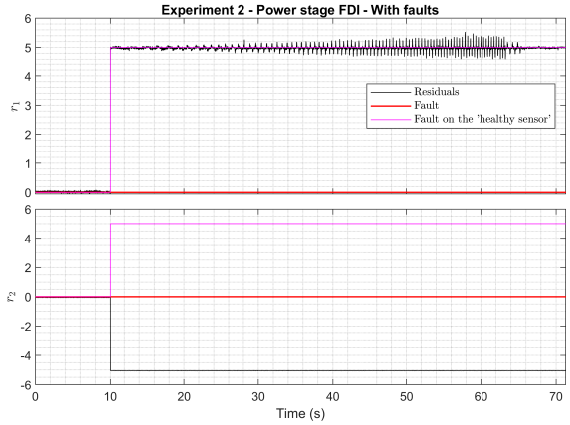

Fig. 17: Power stage residual signals (Experiment #2) in presence of a bias fault affecting the second ("healthy" at synthesis stage) current sensor.

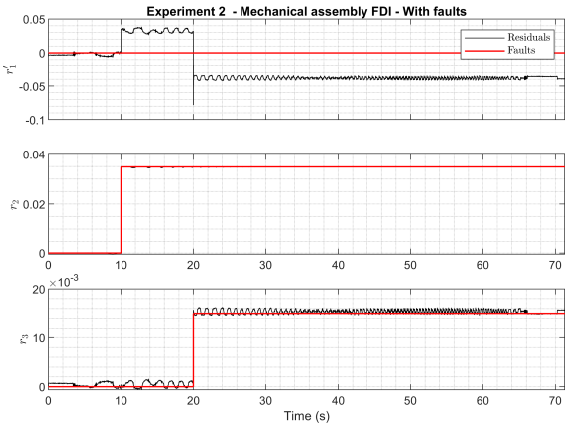

Fig. 18: Mechanical assembly residual signals (Experiment #2) in presence of a bias fault affecting the TVC deflection angle and stroke displacement measurements.

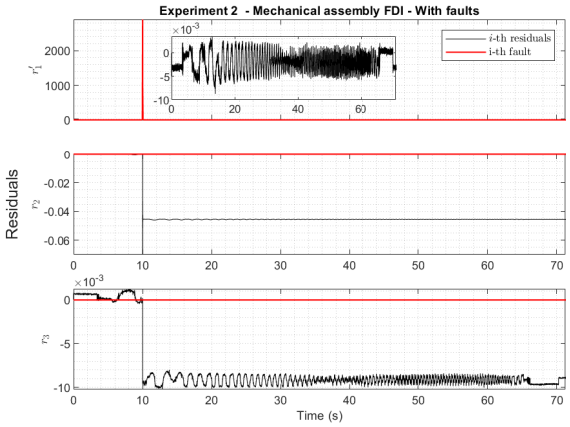

Fig. 19: Mechanical assembly residual signals (Experiment #2) in presence of a bias fault affecting the electrical motor angular position measurement.

observable that the two fault signals are detected and isolated correctly by $r_{2,\mathrm{MA}}$ and $r_{3,\mathrm{MA}}$ residuals respectively, while $r'_{1,\mathrm{MA}}$ is also raising from the zero neighborhood, as expected. Note that after 20 seconds, nothing can be said about which sensor is faulty, since all the residuals are far from zero. In Fig. 19, we inject a bias of 4 revolutions as fault acting on θ measurement: this value is chosen because of the very low transmission ratio L_g and the high noise of the potentiometer, which would impede the evaluation of the residual signal. No fault is injected in the other two sensors. It can be observed that such abrupt bias injection generates a very high deviation of $\dot{\theta}$, highlighted in red. However, in the zoomed box, one can see that the residual value keeps low regardless of the fault $\dot{\theta}$ measurement. On the other hand, the r_2 and r_3, both depending on θ, would highlight the presence of a fault. Because r'_1 keeps close to zero, we can therefore correctly identify that the fault is due to a degraded motor angular position sensor.

7. Conclusions

In this paper, we addressed the synthesis of fault detection and isolation (FDI) algorithms for monitoring the

sensors of a reusable rocket's Thrust Vector Control (TVC) system based on Electro-Mechanical Actuators (EMAs). The proposed FDI architecture, relying on the nullspace approach, was verified through real testing on an ad-hoc hardware platform. The sensor suite was selected to closely resemble both the actual system and the employed test-bench. The proposed FDI architecture comprises two components: one addressing faults in the power stage and the other targeting faults in the mechanical assembly.

For the power stage, strong fault detectability and isolability were verified. Since sensorless control strategies can be employed when motor current measurements are unavailable, it is important to determine whether a fault is affecting the current sensors or if the power unit itself is faulty. To achieve this, we require at least two current sensors, which are often readily available in high-performance devices. The solution was tested in various fault-free and faulty scenarios using experimental data, demonstrating that the expectations were met.

The FDI testing for the mechanical assembly followed the same principles. Due to the plant structure, disturbances (such as friction and vehicle-induced loads), and the faults to be detected, we demonstrated that fault isolation is limited to one fault at a time. Despite this limitation, the results show that biases affecting the electrical motor position measurement, the nozzle angular deflection measurement, or the EMA stroke position measurement can be correctly identified in the residual signals.

In conclusion, while model-based FDI mechanisms can offer analytical redundancy when hardware redundancy is not possible, limitations exist depending on the plant dynamics, FDI requirements, and available measurements. Including the FDI requirements during the TVC system design stage can help prevent these limitations, which might otherwise only be circumvented by adding sensors or relaxing detection/isolation requirements. The proposed FDI architecture proved effective with the considered setup and can be further refined and enhanced with suitable fault evaluation and decision-making logic.

References

[1] Paolo Baiocco. Overview of reusable space systems with a look to technology aspects. *Acta Astronautica*, 189:10–25, 2021.

[2] Gael Dee, Tillo Vanthuyne, Alessandro Potini, Ignasi Pardos, and Guerric De Crombrugghe. Electromechanical thrust vector control systems for the VEGA-C launcher. In *8th European Conference For Aeronautics And Space Sciences (EUCASS)*, Madrid, Spain, 2019.

[3] Chris Bergin - NSF [@NASASpaceflight]. This is real-time! Raptor 2 wiggling like a champ via its electric TVC (Thrust Vector Control) at SpaceX McGregor.[...] https://t.co/msBRnDaj5S, 2022.

[4] Stefano Farì, David Seelbinder, Stephan Theil, Pedro Simplicio, and Samir Bennani. Sensor fault detection and isolation for electro-mechanical actuators in a reusable launch vehicle TVC system. In *10th European Conference For Aeronautics And Space Sciences (EUCASS)*, Lausanne, Switzerland, 2023.

[5] Daniel Ossmann and Franciscus L. J. van der Linden. Advanced sensor fault detection and isolation for electro-mechanical flight actuators. In *2015 NASA/ESA Conference on Adaptive Hardware and Systems (AHS)*, pages 1–8, Montreal (QC), Canada, 2015. IEEE.

[6] Daniel Ossmann, Hans-Dieter Joos, and Philippe Goupil. Enhanced Sensor Monitoring to Maintain Optimal Aircraft Handling in Case of Faults. *Journal of Guidance, Control, and Dynamics*, 40(12):3127–3137, 2017.

[7] Stefano Farì, David Seelbinder, Stephan Theil, Pedro Simplicio, and Samir Bennani. Physical modeling and simulation of electro-mechanical actuator-based TVC systems for reusable launch vehicles. *Acta Astronautica*, 214:790–808, 2024.

[8] Philippe Saunois, Jean-Christophe Verdier, Nicolas Luquet, Nicolas Salvat, and Alexandre Delcausse. Electromechanical TVC using direct engine deflection measurement feedback for reusable stages. In *EUCASS 23*, Lausanne, Switzerland, 2023.

[9] Cédric Renault. Usefulness of a force feedback on electromechanical actuator. In *6th International ESA Conference on Guidance, Navigation and Control Systems*, Loutraki, Greece, 2005.

[10] R. Krishnan. *Permanent Magnet Synchronous and Brushless DC Motor Drives*. CRC Press, Boca Raton (FL), USA, 1 edition, 2017.

[11] Andreas Varga. *Solving Fault Diagnosis Problems*, volume 84 of *Studies in Systems, Decision and Control*. Springer International Publishing, Cham, 2017.

[12] Daniel Ossmann. Optimization based Tuning of Fault Detection and Diagnosis Systems for Large Transport Aircraft. In *ONERA-DLR Aerospace Symposium - ODAS*, 2012.